an Atmospheric Arc Plasma," *Journal of Quantitative Spectroscopy and Radiative Transfer*, Vol. 11, No. 2, Feb. 1971, pp. 291–307.

[6] Lukens, L. A. and Incropera, F. P., "Electric Field Intensity and Wall Heat Transfer Measurements for the Heating Region of an Atmospheric Cascade Arc," *International Journal of Heat and Mass Transfer*, Vol. 15, No. 5, May 1972, pp. 935–952.

[7] Uhlenbusch, J., Fischer, E., and Hackmann, J., "Untersuchungen von Nichtgleichgewichtseffekten an stationären Heliumplasmen," *Zeitschrift für Physik*, Vol. 238, No. 2, Feb. 1970, pp. 404–420.

[8] Kruger, C. H., "Nonequilibrium in Confined-Arc Plasmas," *The Physics of Fluids*, Vol. 13, No. 7, July 1970, pp. 1737–1746.

[9] Incropera, F. P. and Viegas, J. R., "Nonequilibrium in an Arc Constrictor," *AIAA Journal*, Vol. 8, No. 9, Sept. 1970, pp. 1722–1724.

[10] Clark, K. J. and Incropera, F. P., "Thermochemical Nonequilibrium in an Argon Constricted Arc Plasma," *AIAA Journal*, Vol. 10, No. 1, Jan. 1972, pp. 17–18.

[11] Scott, R. K., "Thermochemical Nonequilibrium in Atomic Hydrogen at Elevated Temperatures," Rept. HTGDL-8, Dec. 1972, Purdue Univ., Lafayette, Ind.

[12] Devoto, R. S., "Transport Coefficients of Partially Ionized Hydrogen," *Journal of Plasma Physics*, Vol. 2, No. 4, Dec. 1968, pp. 617–631.

[13] Hinnov, E. and Hirschberg, J. G., "Electron-Ion Recombination in Dense Plasmas," *Physical Review*, Vol. 125, No. 3, Feb. 1962, pp. 795–801.

[14] Allen, C. W., *Astrophysical Quantities*, University of London, The Athlone Press, London, England, 1955.

[15] Petschek, H. and Byron, S., "Approach to Equilibrium Ionization Behind Strong Shock Waves in Argon," *Annals of Physics*, Vol. 1, 1957, pp. 270–315.

[16] Yos, J. M., "Transport Properties of Nitrogen, Hydrogen, Oxygen and Air to 30,000°K," Rept. RAD TM-63-7, 1963, AVCO Corp., Wilmington, Mass.

[17] Longmire, C. L., *Elementary Plasma Physics*, Interscience, New York, 1963.

[18] Wiese, W. L., Paquette, D. R., and Solarski, J. E., "Profiles of Stark-Broadened Balmer Lines in a Hydrogen Plasma," *Physical Review*, Vol. 129, Pt. 1, 1963, pp. 1225–1232.

[19] Morris, J. C. et al., "Evaluation of High Temperature Gas Transport Properties," CR-575, 1966, NASA.

[20] Steinberger, S., "Messung von Temperaturverteilungen im H_2—Kaskadenbogen bis 27,000°K," *Zeitschrift für Physik*, Vol. 223, 1969, pp. 1–18.

[21] Maecker, H., "Transport Properties in High Power Arcs," ARL 69-0031, 1969, Aerospace Research Labs., Wright-Patterson Air Force Base, Ohio.

[22] Greene, C. S., "Parametric Calculations for the Asymptotic Region of Hydrogen, Helium, Argon, Krypton and Xenon Laminar Constricted Arcs," M.S. thesis, 1972, Purdue Univ., Lafayette, Ind.

DECEMBER 1973 AIAA JOURNAL VOL. 11, NO. 12

Starting Transient of Solid-Propellant Rocket Motors with High Internal Gas Velocities

A. PERETZ,* K. K. KUO,† L. H. CAVENY,‡ AND M. SUMMERFIELD§
Guggenheim Laboratories, Princeton University, Princeton, N.J.

A comprehensive analytical model which considers time and space development of the flowfield in solid-propellant rocket motors with high volumetric loading density is described. The gas dynamics in the motor chamber is governed by a set of hyperbolic partial differential equations, that are coupled with the ignition and flame spreading events, and with the axial variation of mass addition. The flame spreading rate is calculated by successive heating-to-ignition along the propellant surface. Experimental diagnostic studies have been performed with a rectangular window motor (50 cm grain length, 5 cm burning perimeter and 1 cm hydraulic port diameter), using a controllable head-end gaseous igniter. Tests were conducted with AP composite propellant at port-to-throat area ratios of 2.0, 1.5, 1.2, and 1.06, and head-end pressures from 35 to 75 atm. Calculated pressure transients and flame spreading rates are in very good agreement with those measured in the experimental system.

Nomenclature

A_p = cross-sectional area of the port, cm^2
A_t = motor nozzle throat area, cm^2
a = pre-exponential factor in the nonerosive burning rate law, ap^n
b = burning perimeter, cm
c = speed of sound, cm/sec; when with subscript, specific heat, cal/g-°K
c_p = specific heat at constant pressure, cal/g-°K
d_h = hydraulic diameter of the port, cm
E = total stored energy, cal/g
f = friction coefficient, $2g\tau_w/\rho u^2$
g = acceleration of gravity, conversion factor, g-cm/gf-sec^2¶
h_c = local convective heat-transfer coefficient, cal/cm^2-sec-°K
h_{cp} = local convective heat-transfer coefficient over the propellant surface, cal/cm^2-sec-°K
h_{cw} = local convective heat-transfer coefficient over nonpropellant port wall, cal/cm^2-sec-°K
h_f = enthalpy of combustion gas at adiabatic flame temperature, cal/g
h_p = port height (see Fig. 3), cm
J_c = mechanical equivalent of heat, gf-cm/cal
k = erosive burning constant, cm^3-°K/cal
L^* = characteristic length, cm
m_{ig} = igniter mass flow rate, g/sec

Presented as Paper 72-1119 at the AIAA/SAE 8th Joint Propulsion Specialist Conference, New Orleans, La., November 29–December 1, 1972; submitted December 14, 1972; revision received May 25, 1973. Based on work performed under NASA. Grant NGL 31-001-109 monitored by NASA Langley Research Center and the Jet Propulsion Laboratory of the California Institute of Technology.

Index categories: Combustion Stability, Ignition, and Detonation; Solid and Hybrid Rocket Engines; Nozzle and Channel Flow.

* Ph.D. Candidate. Member AIAA.

† Post-Doctoral Research Associate; presently Assistant Professor, Pennsylvania State University, University Park, Pa. Member AIAA.

‡ Senior Member of Professional Staff. Associate Fellow AIAA.

§ Professor of Aerospace Propulsion. Fellow AIAA.

¶ gf denotes unit of gram force.

n = pressure exponent in the nonerosive burning rate law
Pr = Prandtl number
P_w = wetted perimeter of the port, cm
p = static pressure, gf/cm^2
p_t = pressure at the motor-nozzle throat, gf/cm^2
q_l = rate of heat transfer, cal/cm^2-sec
R = specific gas constant for the combustion gases, gf-cm/g-°K
r_0 = nonerosive burning rate of the solid propellant, ap^n, cm/sec
r = burning rate of the solid propellant, including the erosive burning contribution, cm/sec
T = temperature (without subscript, static gas temperature), °K
T_{af} = average film gas temperature, $(T+T_{ps})/2$, °K
T_f = adiabatic flame temperature of the solid propellant, °K
T_{ig} = effective mean temperature of the igniter gas, °K
T_{pi} = initial propellant temperature, °K
T_{ps} = propellant surface temperature, °K
$T_{ps,\,ig}$ = propellant surface temperature, at which propellant ignition occurs, °K
T_{ws} = nonpropellant wall surface temperature, °K
t = time, sec
u = gas velocity, cm/sec
V = volume, cm^3
W = molecular weight of the combustion gases, g/g-mole
x = axial distance from igniter nozzle end, cm
x_E = position at the entrance to the motor nozzle, cm
x_p = position at the entrance to the propellant section (propellant slab leading edge), cm
x_r = distance from the point of impingement of the igniter jet, cm
y = perpendicular distance from the propellant surface into the solid, cm
α = thermal diffusivity, cm^2/sec
β = erosive burning exponent [see Eq. (16)]
γ = ratio of specific heats
ε = a small number in Eq. (22) °K
ε_s = equivalent sand roughness, cm
λ = thermal conductivity, cal/cm-sec-°K
μ = viscosity of the combustion gases, g/cm-sec (poise)
ρ = density (without subscript, gas density), g/cm^3
τ_w = shear stress on the port wall, gf/cm^2
τ_{xx} = normal shear stress, gf/cm^2

Subscripts
E = entrance to motor nozzle (motor chamber aft-end)
es = entrance section
i = initial value
pr = solid propellant (condensed phase)

I. Introduction

PREDICTION and control of the pressure-time history of high-performance solid-propellant rocket motors during the early phases of operation often depend on understanding the complex interactions between such elements as the igniter gas flow, convective heating, flame spreading, the developing flowfield, and erosive burning. Typical design and analysis goals are: 1) to reduce motor-to-motor variations in the starting transients of clustered motors; 2) to extrapolate sea-level motor ignition data to high altitude ignition conditions; 3) to reduce the overpressure that sometimes accompanies ignition; 4) to predict how a design modification will alter performance (e.g., propellant substitution, increased throat area, and propellant surface treatment); 5) to predict the effects of long-term storage on ignition requirements; and 6) to avoid too narrow a margin against hang-fire. The objective of ignition research is to provide a sound basis for defining and achieving the design and development goals with a minimum of expensive motor tests. This study is directed at developing analytical and experimental techniques, that can be applied to achieve the aforementioned goals and objectives.

Many studies have dealt with a particular fundamental process, taking place during the starting of solid-propellant motors, or have focused on practical correlations to facilitate igniter design. The analytical models used in those researches, which were directed at the analysis of the over-all starting transient can be categorized into two major groups: 1) lumped chamber-parameter, or $p(t)$ models,[1-5] and 2) quasi-steady one-dimensional flow, or $p(x)$ models.[6-9] The models of the first group assume uniform pressure and stagnation temperature distributions in the combustion chamber port. In the models of the second type, quasi-steady pressure, temperature, and velocity distributions along the port are supposed at each instant of time during the transient. The flame spreading is treated in various ways: an experimentally determined function of time[1,6-8]; partially or fully instantaneous[2,3]; a linear function of the burning rate[4]; or calculated as a function of the spatially varying heat flux due to changing gas temperature[10] or a boundary-layer development.[5]

Many modern, high-performance solid-propellant motors have high volumetric loading density and small port-to-throat area ratio, frequently combined with large length-to-diameter ratio. These motors, referred to in the paper as HVT (high velocity transient) motors, are characterized by high internal gas velocities, significant axial pressure and temperature gradients, pressure overshoots, and relatively short transient times. The starting transients of the HVT motors are inaccurately predicted and unsatisfactorily analyzed by either one of the aforementioned classes of approaches. Figure 1 shows schematically a typical starting transient of HVT motors compared to that of motors with a high port-to-throat area ratio.

In all aspects of this study, the flowfield and pressure variations with time and axial position [$p(t, x)$ model] are considered and the interactions between processes, such as the developing flowfield, convective heat transfer to the solid propellant, flame spreading, and erosive burning are properly taken into account.

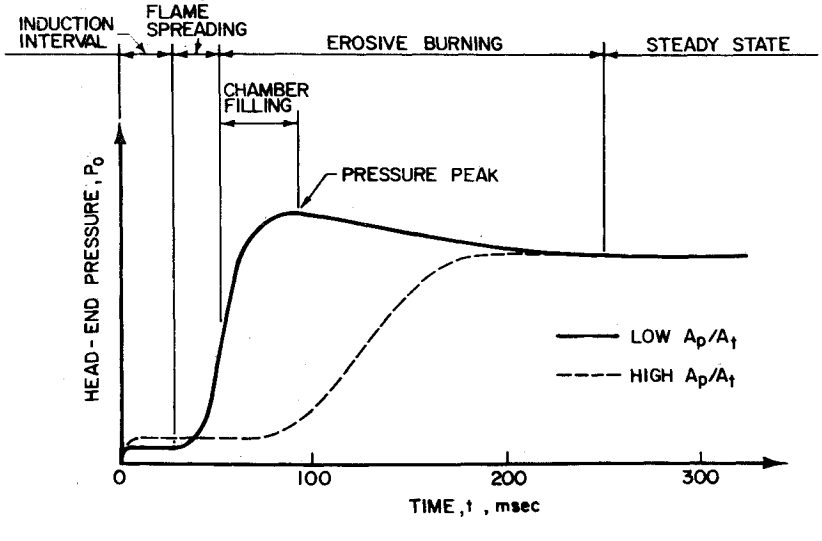

Fig. 1 Typical starting transient of HVT motors (low A_p/A_t) compared with that of motors having high A_p/A_t.

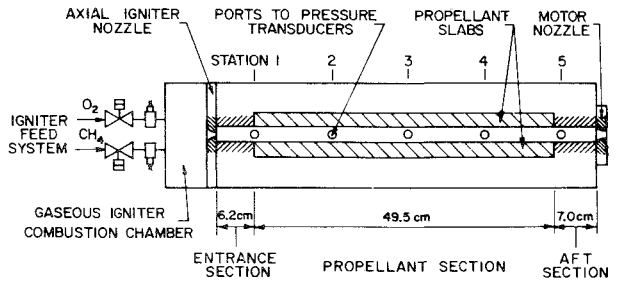

Fig. 2 Experimental rocket motor for starting transient studies.

II. Analysis

A. Description of the Physical Model

The analytical model is established for the general class of HVT motors and is solved for the physical situation, corresponding to the experimental rocket motor, designed and built to provide detailed information on the ignition events and to test the validity of the analytical model.

The physical situation analyzed and solved by the model considers a rectangular window motor, which consists of entrance, propellant, and aft sections (see Fig. 2). Two opposing propellant slabs (2.54 cm wide, 0.635 cm thick, and 49.5 cm long), cast into trays, are positioned in the propellant section. The initial dimensions of the rectangular port [2.54 cm wide and 0.635 cm high (see Fig. 3)] are uniform along the entire motor. The ignition stimulus is provided by a fore-end axial pyrogen igniter, which discharges the ignition gases into the entrance section through a centrally located sonic nozzle. A rectangular replaceable nozzle is attached to the motor aft-end. The entrance and aft sections, and the nonpropellant walls of the port (except the window, when used) are thermally isolated by a thin layer of mixture consisting of 50% PBAA/EPON 828 and 50% TiO_2. This layer ablated only slightly during the starting transient. More details on the experimental facility are given in Sec. III.

At the onset of igniter discharge a flow pattern with pressure, temperature and velocity distributions develops in the motor port. Subsonic flow with friction and heat transfer to the propellant and nonpropellant port walls at low pressure (usually between 1 and 3 atm for the low port-to-throat area ratios under investigation) is established in the chamber. The motor nozzle may be either choked or unchoked. The first phase of the starting transient is the induction interval (ignition lag), which ends with the appearance of the first flame on the propellant surface. The ignition criterion, adopted in this study, is that a point on the propellant surface ignites when it attains some critical ignition temperature,[11] denoted here by $T_{ps,ig}$. Thus the process of flame spreading along the propellant surface, which starts at first ignition and ends when the entire surface is ignited, is described by the model of successive ignitions.[2,3] Once started, the flame spreading is accelerated by the increased heat flux due to the rapidly increasing mass flow originating from the already ignited propellant surface. The transition from unchoked to choked flow is considered in the analysis. Rapid chamber pressurization usually begins with the onset of fast flame spreading. The last phase of the starting transient is the chamber filling period, which follows the completion of flame spreading. Severe erosive burning may take place during this period and thereafter, due to the high gas velocities in the chamber. Thus, the maximum pressure may be much higher than the desired equilibrium pressure. Significant pressure and temperature drops as well as velocity increase are established along the port. Following the pressure peak, a quasi-steady situation develops and pressure decreases toward an equilibrium value due to diminishing erosive burning, as the port area increases.

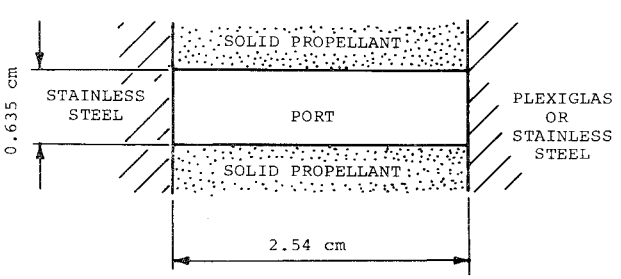

Fig. 3 Cross section of experimental motor, showing port configuration.

B. Basic Assumptions

The following basic assumptions were used in the analytical model:

1) All chemical reactions occur on the propellant surface in a combustion zone, which is so thin that it can be considered as a plane. The combustion products enter the main stream in the port with zero axial momentum.

2) The flow in the chamber port is one dimensional. This assumption is a good approximation to the real situation in view of the highly turbulent flows encountered in HVT motors. Changes of flow properties across the boundary layer are considered in the expressions for heat-transfer and friction coefficients used in the analysis.

3) Rate processes at the propellant surface are quasi-steady in the sense that their characteristic times are short compared to that of the pressure transient.

4) The propellant combustion products and the pyrogen igniter gas have the same values of c_p, W, and γ.

5) The gases flowing in the port obey the perfect gas law.

C. Description of the Analytical Model

Governing equations

A control volume element is established in the motor port, as shown in Fig. 4. The mathematical formulation of the approach to the previously described problem consists of the following: a) mass, momentum, and energy conservation equations in unsteady, quasi-one-dimensional form for the gas phase; b) equation of state for the gas flowing in the motor; c) proper initial conditions at the start of the transient (onset of igniter flow); d) two boundary conditions at the fore-end of the propellant section, obtained from a pair of ordinary differential equations, which describe the rate of change of pressure and

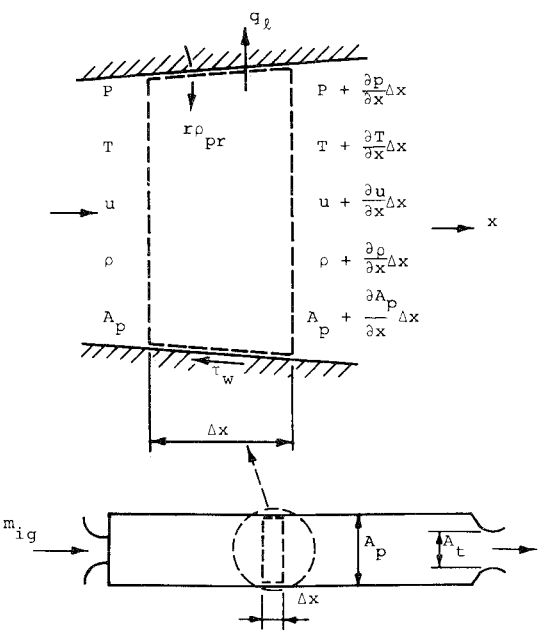

Fig. 4 Analytical control volume.

temperature in the entrance section; e) a third boundary condition, which describes the gas velocity at the entrance to the motor nozzle, for either choked or unchoked flow; f) semi-empirical correlations for the convective heat-transfer and friction coefficients for the highly-turbulent flow in the port; g) burning rate law for the solid propellant, including the effects of initial temperature, pressure, and velocity over the surface (erosive burning); and h) a solid phase heat-up equation for determination of the propellant surface temperature during the induction interval coupled to an ignition criterion for the propellant.

The mass conservation equation for the control volume in Fig. 4, written for a unit volume, is

$$\frac{\partial \rho}{\partial t}+\frac{\partial(\rho u)}{\partial x}+\frac{\rho u}{A_p}\frac{\partial A_p}{\partial x}=\frac{rb}{A_p}(\rho_{pr}-\rho) \tag{1}$$

The momentum conservation equation is

$$\frac{\partial(\rho u)}{\partial t}+\frac{\partial(\rho u^2)}{\partial x}+\frac{\rho u^2}{A_p}\frac{\partial A_p}{\partial x}+\frac{\rho u}{A_p}\frac{\partial A_p}{\partial t}= -g\frac{\partial p}{\partial x}-g\left(\frac{\partial \tau_{xx}}{\partial x}+\frac{\tau_{xx}}{A_p}\frac{\partial A_p}{\partial x}\right)-g\frac{\tau_w P_w}{A_p} \tag{2}$$

The energy conservation equation, written in terms of the total stored (internal and kinetic) energy per unit mass, E, is

$$\frac{\partial(\rho A_p E)}{\partial t}+\frac{\partial(\rho A_p u E)}{\partial x}=\frac{\partial}{\partial x}\left(\lambda A_p\frac{\partial T}{\partial x}\right)-\frac{1}{J_c}\frac{\partial(A_p up)}{\partial x}-\frac{1}{J_c}\frac{\partial}{\partial x}(\tau_{xx}A_p u)+\rho_{pr}brh_f-q_l P_w \tag{3}$$

The preceding conservation equations constitute a set of inhomogeneous, nonlinear, partial differential equations. After nondimensionalization and an order of magnitude analysis, the effects of the following terms were neglected: a) rate of mass accumulation in the free volume created by the propellant surface regression (as compared to the rate of mass addition due to burning); b) forces between gas molecules due to the viscous stress in the axial direction, created by the axial velocity gradient; c) viscous dissipation and rate of work done by the internal viscous forces; and d) axial heat conduction between gas molecules. The wall friction at a station in the propellant section is neglected when the ignition temperature is reached and appreciable blowing starts.

After rearrangement of the mass and energy conservation equations, and using the perfect gas equation of state, the following set of governing equations is obtained:

$$\frac{\partial u}{\partial t}+u\frac{\partial u}{\partial x}+gR\frac{T}{p}\frac{\partial p}{\partial x}=-\frac{\rho_{pr}brR}{A_p}\frac{Tu}{p}-\frac{fP_w}{2A_p}u^2 \tag{4}$$

$$\frac{\partial T}{\partial t}+u\frac{\partial T}{\partial x}+(\gamma-1)T\frac{\partial u}{\partial x}=-\frac{(\gamma-1)uT}{A_p}\frac{\partial A_p}{\partial x}+\gamma R\rho_{pr}\frac{br}{A_p}\frac{T}{p}\left(T_f-\frac{T}{\gamma}+\frac{u^2}{2gJ_c c_p}\right)-(\gamma-1)\frac{P_w}{A_p}\frac{T}{P}\left(J_c q_l-\frac{fpu^3}{2gRT}\right) \tag{5}$$

$$\frac{\partial p}{\partial t}+u\frac{\partial p}{\partial x}+\gamma p\frac{\partial u}{\partial x}=-\frac{\gamma pu}{A_p}\frac{\partial A_p}{\partial x}+(\gamma-1)\frac{\rho_{pr}br}{A_p}\left(J_c c_p T_f+\frac{u^2}{2g}\right)-\frac{(\gamma-1)P_w}{A_p}\left(J_c q_l-\frac{f}{2g}\frac{pu^3}{RT}\right) \tag{6}$$

The following expression for the rate of heat loss to the propellant and nonpropellant walls, q_l, pertinent to the physical and experimental configuration (see Fig. 3) was used in the analysis:

$$q_l=[2h_{cw}h_p(T-T_{ws})+h_{cp}b(T-T_{ps})]/P_w \tag{7}$$

The three governing equations [Eqs. (4–6)] are first-order, inhomogeneous, coupled and nonlinear partial differential equations. The independent variables are time t, and distance along the port x, and the unknowns are the gas velocity u, temperature T, and pressure p.

The three necessary initial conditions describing a state of uniform distribution in the propellant and aft sections of the motor are:

$$u(0,x)=u_i,\quad T(0,x)=T_i,\quad p(0,x)=p_i \tag{8}$$

where u_i, T_i, and p_i are the initial gas velocity, temperature, and pressure in the motor. To facilitate the start of the numerical solution, it is assumed that p_i is slightly higher than the ambient pressure (by 0.0001 atm), with resulting small velocity u_i in the port.

The three physical boundary conditions are as follows: two boundary conditions at the entrance to the propellant section (denoted by x_p), and one boundary condition at the entrance to the motor nozzle (denoted by x_E).

The gas properties in the entrance section are assumed to be uniform. Heat-transfer and shock-pattern losses taking place there are found to lower the effective mean temperature of the igniter gas T_{ig}.[12–14] From the continuity and energy conservation equations for the entrance section, the following equations, expressing the rate of change of pressure and temperature at the entrance to the propellant section are derived:

$$\frac{dp_{es}}{dt}=\frac{1}{V_{es}}\left[\gamma RT_{ig}m_{ig}(t)-\gamma A_{p,es}p_{es}(t)u_{es}(t)-\frac{(\gamma-1)A_{p,es}p_{es}(t)u_{es}(t)^3}{2gRT_{es}(t)}\right] \tag{9}$$

$$\frac{dT_{es}}{dt}=\frac{1}{V_{es}}\left\{\frac{RT_{es}(t)m_{ig}(t)}{p_{es}(t)}[\gamma T_{ig}-T_{es}(t)]-(\gamma-1)A_{p,es}u_{es}(t)\left[T_{es}(t)+\frac{u_{es}(t)^2}{2gR}\right]\right\} \tag{10}$$

The igniter mass flow rate m_{ig} is a prescribed function of time, determined from the experimental study.

Equations (9) and (10) form a pair of coupled ordinary differential equations for the unknowns p_{es} and T_{es}. Their solution provides two boundary conditions for the governing Eqs. (4–6). The two initial conditions for this pair of equations are

$$p_{es}(0)=p_{es,i}\quad\text{and}\quad T_{es}(0)=T_{es,i} \tag{11}$$

The boundary condition at the aft end of the motor chamber is derived assuming isentropic flow between the entrance to the motor nozzle and the nozzle throat. Using continuity and energy conservation relations between these two sections, the following equation is derived:

$$u_E(t)^2=\frac{2g\gamma}{\gamma-1}RT_E(t)\frac{1-[p_t(t)/p_E(t)]^{(\gamma-1)/\gamma}}{(A_p/A_t)^2[p_t(t)/p_E(t)]^{-2/\gamma}-1} \tag{12}$$

When the motor nozzle is unchoked (the usual case during the induction intervals, when very low port-to-throat area ratios are used) the pressure at the nozzle throat, p_t in Eq. (12), equals the ambient pressure. For the case of a choked motor nozzle Eq. (12) becomes the following implicit relation:

$$u_E(t)^2=\frac{\gamma gRT_E(t)}{[A_p/A_t]^2}\left[\frac{2}{\gamma+1}\right]^{(\gamma+1)/(\gamma-1)}\times\left[1+\frac{\gamma-1}{2}\frac{u_E(t)^2}{\gamma gRT_E(t)}\right]^{(\gamma+1)/(\gamma-1)} \tag{13}$$

Empirical correlations for the heat-transfer and friction coefficients

The expression for the local convective heat-transfer coefficient h_c is deduced from the conventional Dittus-Boelter correlation for turbulent flow in pipes. Entrance effects, observed by many investigators[12–16] are accounted for by including a power function of the length-to-diameter ratio.[16,17] Variation of the gas physical properties across the boundary layer is considered by evaluating the properties at an average film temperature T_{af}.[15,18] The expression for h_c, used in the study,[17] is

$$h_c=1.56\times10^{-3}Pr^{-0.6}c_p(pu/R)^{0.8}\times W^{0.1}T_{af}{}^{-0.67}(x_r d_h)^{-0.1}(A_p/A_t)^{0.4} \tag{14}$$

Before local ignition $h_{cp} = h_{cw} = h_c$, whereas after local ignition $h_{cp} = 0$ and $h_{cw} = h_c$.

The friction coefficient f is deduced from Colebrook's expression for turbulent flow in pipes with roughness.[19] Observed entrance effects[20] and variation of fluid properties across the boundary layer[16] are taken into account. The friction factor is expressed in the following form[17]:

$$f = \frac{0.449(d_h/x_r)^{0.1}}{\left\{\ln\left[\frac{\varepsilon_s/d_h}{3.7} + \frac{1.27RW^{0.5}T_{af}{}^{1.65}(d_h/x_r)^{0.05}}{10^6 pud_h f^{0.5}}\right]\right\}^2} \quad (15)$$

The burning rate law

A modified Lenoir-Robillard's burning rate law[21,22] is used to account for erosive burning:

$$r = ap^n + kh_c \exp(-\beta r\rho_{pr}/u\rho) \quad (16)$$

where the erosive burning constant k is estimated from theoretical considerations,[20] the zero-blowing heat-transfer coefficient h_c is calculated according to Eq. (14), and the erosive burning exponent β is evaluated from water-quench experiments (by

$$\int_0^t r\,dt$$

vs x measurements after extinguishment shortly after the transient), and adjusted to fit the experimental pressure-time curves for all values of A_p/A_t tested.

Determination of the propellant surface temperature

The heat equation for an unignited propellant grain at a fixed axial location is

$$\partial T_{pr}(t, y)/\partial t = \alpha_{pr}\partial^2 T_{pr}(t, y)/\partial y^2 \quad (17)$$

with the following initial and boundary conditions:

$$T_{pr}(0, y) = T_{pi} \quad (18)$$

$$T_{pr}(t, \infty) = T_{pi} \quad (19)$$

$$\partial T_{pr}(t, 0)/\partial y = -[h_c(t)/\lambda_{pr}][T(t) - T_{ps}(t)] \quad (20)$$

To determine the propellant surface temperature T_{ps}, Eq. (17) must be solved together with the governing equations for the gas phase. Equation (17) is solved for the surface temperature using an integral method.[23] A third-degree polynomial in y was used to represent the transient temperature profile in the solid phase; using the proper boundary conditions, the following ordinary differential equation for the propellant surface temperature at each prescribed axial position is obtained[17]:

$$\frac{dT_{ps}}{dt} = \frac{4\alpha_{pr}h_c{}^2(T - T_{ps})^3}{3\lambda_{pr}{}^2(T_{ps} - T_{pi})(2T - T_{ps} - T_{pi})} \quad (21)$$

To avoid the singularity at $t = 0$, the initial condition for Eq. (21) is taken as

$$T_{ps}(0) = T_{pi} + \varepsilon \quad (22)$$

where ε has a small value, e.g., 0.1°K.

Equation (21) is solved simultaneously with the governing equations for the chamber flowfield to yield the propellant surface temperature at any calculated time and position. In this way flame spreading rates can be predicted, using a proper ignition criterion.

The large number of coupled parameters, involved in the analysis, precludes a simple and useful nondimensionalization. Moreover, it is doubtful, if any use of normalized parameters can provide an easy and straightforward interpretation of the results. Therefore, it was decided to carry on the numerical calculations in a dimensional form, using consistent, metric engineering system of units, thus allowing a direct comparison of predictions with experimental measurements.

D. Numerical Solution

A computer program was implemented to obtain numerical solutions of the analytical model by the simultaneous integration of the three governing equations (4–6), the two equations for the entrance section, Eqs. (9) and (10), and the propellant surface temperature equation (21). The set of governing equations is found to be hyperbolic in nature, and its numerical solution is based on central differences in space (x) and generalized implicit differences in time (t).[24] A quasi-linearization method,[25] used to linearize the inhomogeneous terms of the governing equations, is combined with a predictor-corrector procedure to assure efficient computation, improve stability and minimize the error.

The utilization of central-difference formulation requires three extraneous boundary conditions in addition to the ones given by Eqs. (9, 10, and 12 or 13). They are derived from the compatibility relations at the boundaries, i.e., by solving the governing equations by the method of characteristics at the boundaries.

The compatibility relation along the right-running Mach line (defined by $dx/dt = u + c$), taking into account the conditions at the right boundary, is

$$\left(\frac{dp}{dt}\right)_1 = -\frac{\gamma p}{c}\left(\frac{du}{dt}\right)_1 + \frac{P_w}{A_p}\left\{\frac{\gamma}{2}\frac{fpu^2}{c}\left[(\gamma-1)\frac{u}{c} - 1\right] - (\gamma-1)J_c h_{cw}(T - T_{ws})\right\} \quad (23)$$

The relation along the left-running Mach line (defined by $dx/dt = u - c$) is

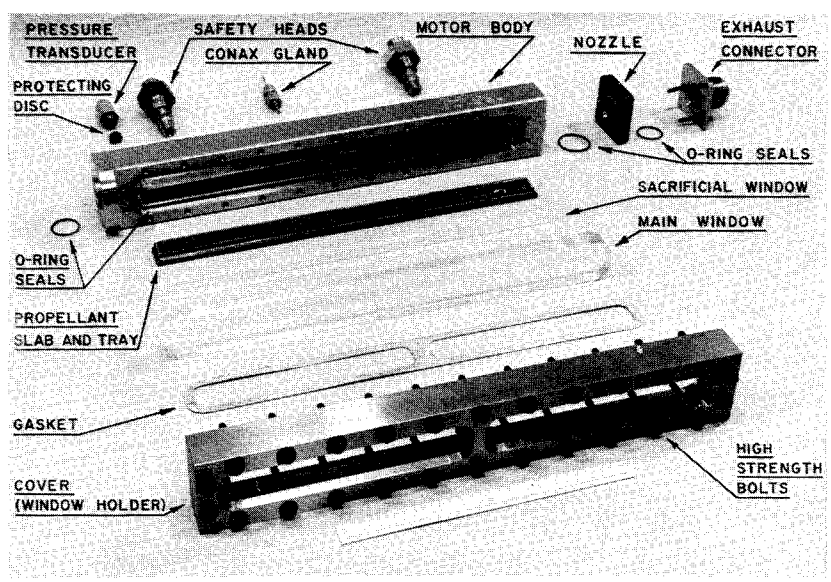

Fig. 5 Exploded view of experimental window motor.

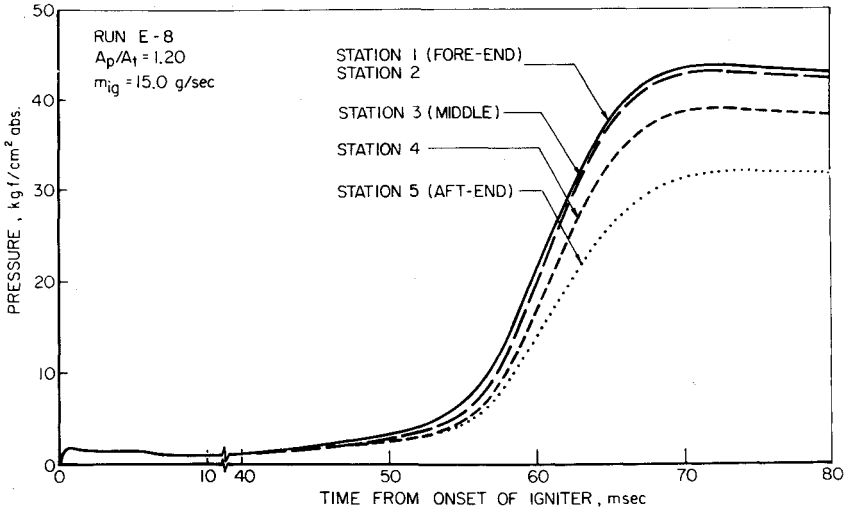

Fig. 6 Pressure transients recorded during starting period at five different stations along the port, showing negative pressure-distance gradient.

$$\left(\frac{dp}{dt}\right)_{II} = \frac{\gamma p}{c}\left(\frac{du}{dt}\right)_{II} + \gamma R\rho_{pr}\frac{rb}{A_p}\left(T_f + \frac{u}{c}T\right) + (\gamma-1)\rho_{pr}\frac{rb}{A_p}\frac{u^2}{2g} - \frac{\gamma pu}{A_p}\frac{\partial A_p}{\partial x} - \frac{(\gamma-1)J_c}{A_p}[2h_p h_{cw}(T-T_{ws}) + bh_{cp}(T-T_{ps})] + \frac{\gamma}{2}\frac{P_w f}{A_p}\frac{pu^2}{c^2}[(\gamma-1)u+c] \quad (24)$$

The relation along the particle-path line (defined by $dx/dt = u$) is

$$\left(\frac{dT}{dt}\right)_{III} = \frac{\gamma-1}{\gamma}\frac{T}{p}\left(\frac{dp}{dt}\right)_{III} + \frac{\gamma-1}{\gamma}\frac{P_w}{A_p}\left[\frac{fu^3}{2gR} - J_c h_{cw}\frac{T}{p}(T-T_{ws})\right] \quad (25)$$

The compatibility relation, Eq. (24), and Eqs. (9) and (10) form a closed system to determine the gas velocity, temperature and pressure at the entrance to the propellant section, whereas the system formed by Eqs. (23) and (25), and Eq. (12) or (13) determines the flow parameters at the chamber aft-end. To prevent numerical oscillations in the boundary-value calculations, each system is solved by the quasi-linearized implicit method.[17]

The governing equations, in their finite-difference form, are arranged in a block-tridiagonal matrix form,[26] which allows an efficient computation. The previously described procedure was organized into a Fortran IV computer program.

III. Experimental Set-Up

An experimental program was conducted to perform diagnostic studies, to provide necessary experimental data, and to verify the predictions developed from the solution of the analytical model. Figure 5 shows an exploded view of the laboratory-size window motor. The primary feature of the slab-grain geometry is that it permits direct photographic observation during ignition and flame spreading and at the same time the chamber conditions realistically correspond to the conditions in a practical rocket motor.

One wall of the port is a two-part Plexiglas window. Tests with fast water quench revealed that no Plexiglas ablation occurs prior to the time of peak pressure. The opposite wall of the port channel is used for the instrumentation ports. Five Dynisco PT76 high-frequency pressure transducers can be installed along the port, 12.7 cm apart. A burst diaphragm is connected to each end of the motor for overpressure protection. Three additional ports are available for thermocouple probes and heat-flux gages. The copper nozzle consists of a rectangular convergent section and a precisely defined rectangular throat.

The ignition system used in the study is a versatile, controllable pyrogen gaseous igniter, which burns pure hydrocarbon fuel (usually methane) and oxygen. The specially-designed igniter combustion chamber achieves 80% of the equilibrium conditions within 3 msec. The injector head comprises two carefully calibrated pairs of unlike impingement orifices. Control devices permit a wide-range variation of the igniter mass flow rate, temperature, and duration. The gaseous igniter was usually operated with an equivalence ratio ranging between 1.02 and 1.08.

IV. Discussion of Results

Diagnostic experimental tests and corresponding computer calculations were conducted with AP composite propellant at port-to-throat area ratios of 2.0, 1.5, 1.2, and 1.06. Pressure measurements, water quench, and high-speed photography have

Table 1 Baseline values

Propellant properties:	
Composition: 20% PBAA-EPON 828	
80% AP (30% 15 mic. & 70% 180 mic.)	
$r_{0\,@\,p=68\,atm}$	= 0.804 cm/sec = 0.32 in./sec
n	= 0.4
λ_{pr}	= 0.9×10^{-3} cal/cm-sec-°K
ρ_{pr}	= 1.6 g/cm³
α_{pr}	= 0.1875×10^{-2} cm²/sec
W	= 22.01 g/g-mole
γ	= 1.24
μ	= $0.87\times10^{-6}\,W^{0.5}T^{0.65}$ poise
c_p	= 0.4665 cal/g-°K
R	= 3852 gf-cm/g-°K
$T_{ps,ig}$	= 700°K
T_f	= 2225°K
T_{pi}	= 298°K
k	= 5.72 cm³-°K/cal
β	= 105
ε_s	= 0.001 cm
Motor parameters:	
x_p	= 6.2 cm
b	= 5.08 cm
$A_{p,i}$	= 1.61 cm²
L^*	= 62.7 (A_p/A_t) cm
x_E	= 62.7 cm
$d_{h,i}$	= 1.02 cm
$P_{w,i}$	= 6.35 cm

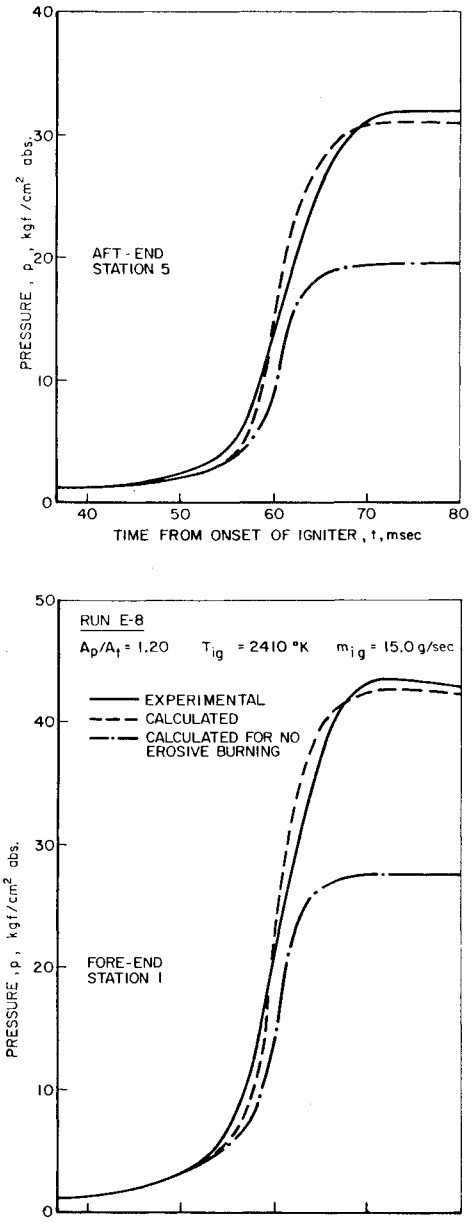

Fig. 7 Agreement of measured and calculated pressure vs time traces at fore-end and aft-end of rocket motor. Demonstration of contribution of erosive burning.

been used to study such phenomena as $p(t, x)$ variations, ignition delays, flame spreading, and erosive burning. Table 1 defines the baseline values used in the calculations. These values correspond closely to the experimental conditions in all tests.

Figure 6 shows typical starting transient $p(t, x)$ measurements during an experimental test, designated as Run E-8 with $A_p/A_t = 1.2$. Following a small pressure wave, caused by the onset of igniter flow, an almost uniform pressure distribution at 1.2 atm absolute is established in the motor cavity. At 36 msec after the igniter start, a flame is observed (on high-speed photographs) at the leading edges of the propellant slabs and flame spreading begins. The measured time-dependence of the pressure distribution is depicted in Fig. 6, which shows the pressure-time history at the five measurement stations denoted in Fig. 2. As expected, because of the low Mach numbers near the fore-end, the measured pressures at station 2 are identical to those at station 1. The pressure rise at station 3 (middle of motor) starts later but increases at the fastest rate. Pressure peaks are achieved at 72 msec at the fore-end (station 1) and at 73.5 msec at the aft-end (station 5). Comparisons between the measured and

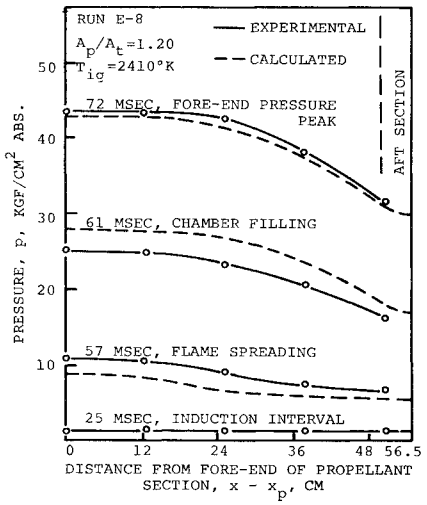

Fig. 8 Comparison of measured and calculated axial pressure distributions at four times during starting transient of Test E-8 within the four significant intervals displayed in Fig. 1.

calculated (by the analytical model) pressure-time curves at stations 1 and 5 are shown in Fig. 7. An excellent agreement between the two curves, including the initial development of pressure distribution, exists during the induction interval (not shown in Fig. 8). Ignition at the propellant leading edge is precisely predicted. During the flame spreading period, the calculated pressure is slightly lower than the measured pressure, whereas during chamber filling the calculated pressure is slightly higher than the measured pressure. There is very good agreement between calculated and measured pressure-peak values at all stations.

Measured and calculated spatial pressure distributions at four illustrative times of Run E-8 are compared in Fig. 8. Calculated spatial velocity and temperature distributions at the same times are ploted in Figs. 9 and 10, respectively.

Agreement within 10% was obtained between calculated and experimentally observed ignition delay times using the modified pipe-flow heat-transfer correlation. However, a careful estimation of the effective mean temperature, T_{ig}, of the igniter gas in the entrance section was necessary for each test. The estimation was performed with the heat-transfer correlations developed by Cohen et al.[27] from the heat flux measurements of Carlson, Seader, and Wrubel.[12,13] It was found that by including friction

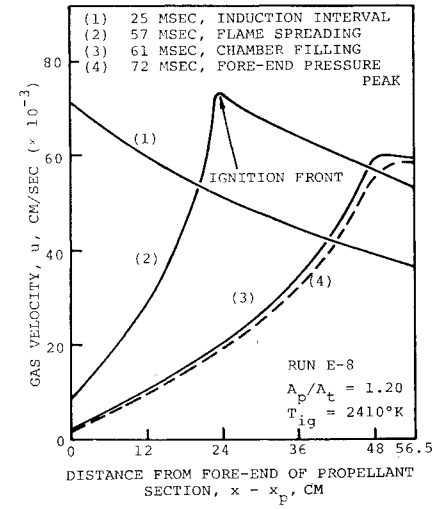

Fig. 9 Calculated axial gas velocity distributions at the same four times as in Fig. 8.

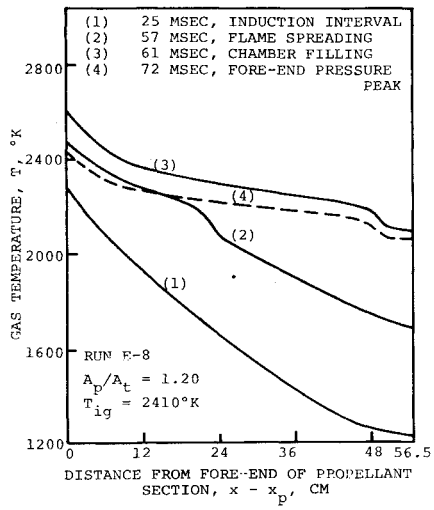

Fig. 10 Calculated axial gas temperature distributions at the same four times as in Fig. 8.

approximately 5% accuracy in calculations of ignition delay and flame spreading times was gained. It should be noted that in many tests, start of pressurization in the motor chamber was measured before any observation of ignition, which may be due to preignition decomposition-gasification of the solid propellant.

High-speed photography of fast flame spreading is a difficult task. Flame spreading appears to be more like an increasing cross-sectional density of ignited points rather than a well-defined advancing flame front. Figure 11 shows calculated and measured locations of the flame front vs time for an experimental test with port-to-throat area ratio of 1.5. Flame spreading rates were found to increase with increasing m_{ig} and A_p/A_t. Rates ranging from 930 cm/sec to 19,800 cm/sec at the start and the end of the process, respectively, were obtained for $A_p/A_t = 2.0$ and $m_{ig} = 19.5$ g/sec. For the same igniter mass flow rate and chamber geometry, lower flame spreading rates are obtained with lower port-to-throat area ratios because the larger throat area results in lower pressure (and, thus, lower heat flux and chemical reaction rates) prior to the chamber filling phase.

For all port-to-throat area ratios tested, the highest pressurization rates were measured in station 3 (middle of motor). For the same motor chamber geometry used in this study, the maximum pressurization rate increases slightly with igniter mass flow rate in the range tested (10 to 21.5 g/sec) and increases considerably with increasing port-to-throat area ratio. Fore-end pressurization

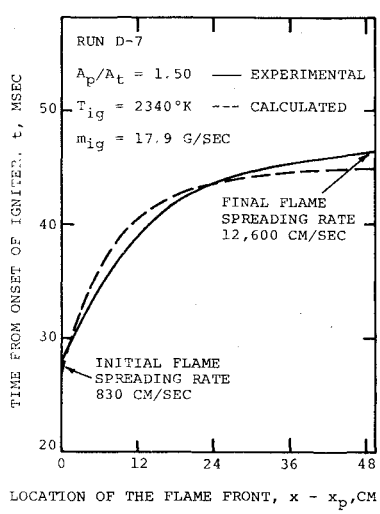

Fig. 11 Measured and calculated ignition flame front locations vs time, with flame spreading velocities noted.

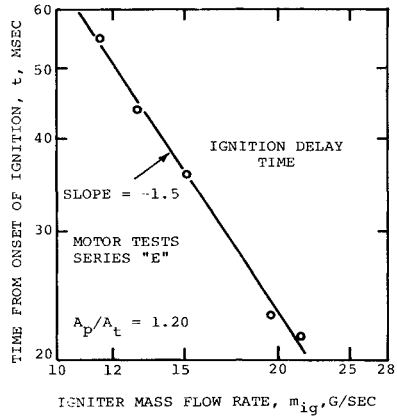

Fig. 12 Measured times of ignition delay for $A_p/A_t = 1.2$.

rates as high as 6800 atm/sec with $A_p/A_t = 2.0$ and as low as 3000 atm/sec with $A_p/A_t = 1.06$ were measured.

Detailed experimental, as well as theoretical parametric studies, were conducted to determine effects of parameters such as igniter gas temperature, igniter mass flow rate, and port-to-throat area ratio on values of interest such as ignition delay times, flame spreading rates, pressurization rates, and peak pressures. Figure 12 shows the measured effect of igniter mass flow rate on ignition delay time for series of tests with port-to-throat area ratio of 1.2. The slope of the log-log plot of ignition delay time vs igniter mass flow rate in Fig. 12 is very close to the slope deduced from turbulent flow correlations, which shows that turbulent flow (although not fully developed), exists over the leading edge of the propellant slabs.

V. Conclusions

A successful analytical model was developed to describe the starting pressure transient of monolithic solid-propellant rocket motors with low port-to-throat area ratios, resulting in high internal gas velocities. Velocity, pressure, and temperature distributions can now be calculated as a function of time and axial distance. The pressure transients calculated by the analytical model are in close agreement with the $p(t, x)$ measurements in the experimental motor. Ignition delay times, flame spreading rates, pressure peaks, and times to achieve the pressure peaks are accurately predicted. In addition, the analytical model can be modified for application to various types of practical solid propellants and operational motor configurations (such as segmented motors). The model can be readily extended to motors using propellants with low aluminum content and fine aluminum particle size by using effective values of the gas properties. However, for highly aluminized propellants (which form large Al/Al_2O_3 agglomerates) it may be necessary to include in the model time and space-dependent particle drag forces (with the proper distribution function) and combustion in the main stream.

In comparison with previous studies as reviewed by Most and Summerfield in Ref. 5, the essential new elements in this study are: 1) techniques to account for the strong contribution of erosive burning, coupled to the chamber gas dynamics; 2) ability to consider significant pressure, temperature, and velocity spatial gradients, encountered in HVT motors, and their variation with time during the starting transient; and 3) calculation of the propellant surface heat-up to ignition, coupled to both temporal and spatial changes of flow parameters in the chamber. Indeed, to account for the experimentally observed steep pressure rise and pressure overshoots, the dominant influences of erosive burning and the spatial gradients of pressure, temperature, and velocity must be accurately taken into account.

When more precise agreement between the analytical calculations and experimental measurements is required in particular investigations, it can be obtained by using more comprehensive correlations for the convective heat transfer and burning rate, by taking into account effects such as increased heat transfer to

rough propellant surfaces, attenuation of heat transfer by the "blowing" at the propellant surface due to preignition gasification, unsteady burning resulting from preheating during the induction interval and high pressurization rates during the fast pressure rise, and turbulent boundary-layer structure.

The experimental system can be readily used to conduct various diagnostic tests pertinent to modern rocket motors, e.g., heat-flux measurements, start-stop control, propagation of pressure perturbations, and liquid-quench extinguishment.

The results of this study are useful to designers of high-performance solid-propellant motors. In particular, by using the techniques presented in this paper, the designer can prescribe the upper limit of volumetric loading density, that can be safely specified, and predict more accurately the pressure-thrust-time motor performance during the starting transient.

References

[1] Adams, D. M., "Igniter Performance in Solid-Propellant Rocket Motors," *Journal of Spacecraft and Rockets,* Vol. 4, No. 8, Aug. 1967, pp. 1024–1029.

[2] DeSoto, S. and Friedman, H. A., "Flame Spreading and Ignition Transients in Solid Grain Propellants," *AIAA Journal,* Vol. 3, No. 3, March 1965, pp. 405–412.

[3] Parker, K. H., Most, W. J., and Summerfield, M., "The Ignition Transient in Solid-Propellant Rocket Motors," *Astronautica Acta,* Vol. 12, No. 4, July–Aug. 1966, pp. 245–257.

[4] Bradley, H. H., Jr., "Theory of a Homogeneous Model of Rocket Motor Ignition Transients," AIAA Paper 64-127, Palo Alto, Calif., 1964.

[5] Most, W. J. and Summerfield, M., "Starting Thrust Transients of Solid Rocket Engines," Aerospace and Mechanical Sciences Report 873, July 1969, Princeton Univ., Princeton, N.J.

[6] Threewit, T. R., Rossini, R. A., and Uecker, R. L., "The Integrated Design Computer Program and the ACP-1103 Interior Ballistics Computer Program," Rept. STM-180, Dec. 1964, Aerojet-General Corp., Sacramento, Calif.

[7] Barron, J. G., Jr., Cook, K. S., and Johnson, W. C., "Grain Design and Internal Ballistics Evaluation Program (IBM 7094 Fortran IV)," Program 64101, June 1967, Hercules Powder Co., Bacchus Works, Magna, Utah.

[8] Vellacott, R. J. and Caveny, L. H., "A Computer Program for Solid Propellant Rocket Motor Design and Ballistic Analysis," ARS Preprint 2315-62, Waco, Texas, Jan. 1962.

[9] Miller, W. H. and Barrington, D. K., "A Review of Contemporary Solid Rocket Motor Performance Prediction Techniques," *Journal of Spacecraft and Rockets,* Vol. 7, No. 3, March 1970, pp. 225–237.

[10] Brown, R. S., Wirrick, T. K., and Anderson, R., "Theory of Ignition and Ignition Propagation of Solid Propellants in a Flow Environment," AIAA Paper 64-157, Palo Alto, Calif., 1964.

[11] Summerfield, M., Parker, K. H., and Most, W. J., "The Ignition Transient in Solid Propellant Rocket Motors," Aerospace and Mechanical Sciences Report 769, Feb. 1966, Princeton Univ., Princeton, N.J.

[12] Carlson, L. W. and Seader, J. D., "Heat Transfer Characteristics of Hot-Gas Ignition," *AIAA Journal,* Vol. 5, No. 7, July 1967, pp. 1272–1279.

[13] Wrubel, J. A. and Carlson, L. W., "Study of Heat Transfer Characteristics of Hot-Gas Igniters," AFRPL-TR-67-267, July 1967, Rocketdyne, Canoga Park, Calif.

[14] Falkner, C. E. and Miller, C. L., "Analytical Igniter Design for Solid Propellant Rocket Motors," AFRPL-TR-70-69, May 1970, CETEC Corp., Mountain View, Calif.

[15] Kilgroe, J. D., "Studies on Ignition and Flame Propagation on Solid Propellants," UTC 2229-FR, Nov. 1967, United Technology Center, Sunnyvale, Calif.

[16] Humble, L. V., Lowdermilk, W. H., and Desmon, L. G., "Measurements of Average Heat-Transfer and Friction Coefficients for Subsonic Flow of Air in Smooth Tubes at High Surface and Fluid Temperatures," Rept. 1020, 1951, NASA.

[17] Peretz, A., "The Starting Transient of Solid-Propellant Rocket Motors with High Internal Gas Velocities," Ph.D. thesis, April 1973, AMS Dept., Princeton Univ., Princeton, N.J.

[18] Bartz, D. R., "A Simple Equation for Rapid Estimation of Rocket Nozzle Convective Heat Transfer Coefficients," *Jet Propulsion,* Vol. 27, No. 1, Jan. 1957, pp. 49–51.

[19] Streeter, V. L., *Fluid Mechanics,* 3rd ed., McGraw-Hill, New York, 1962, pp. 213–222.

[20] Shapiro, A. H. and Smith, R. D., "Fricton Coefficients in the Inlet Length of Smooth Round Tubes," TN 1785, Nov. 1948, NACA.

[21] Lenoir, J. M. and Robillard, G., "A Mathematical Method to Predict the Effects of Erosive Burning in Solid Propellant Rockets," *Sixth Symposium (International) on Combustion,* Reinhold, New York, 1957, pp. 663–667.

[22] Lawrence, W. J., Matthews, D. R., and Deverall, L. I., "The Experimental and Theoretical Comparison of the Erosive Burning Characteristics of Composite Propellants," AIAA Paper 68-531, Atlantic City, N.J., 1968.

[23] Goodman, T. R., "Application of Integral Methods to Transient Nonlinear Heat Transfer," *Advances in Heat Transfer,* Vol. 1, Academic Press, New York, 1964, pp. 51–122.

[24] Kuo, K. K., Vichnevetsky, R., and Summerfield, M., "Generation of an Accelerated Flame Front in a Porous Propellant," AIAA Paper 71-210, New York, 1971.

[25] Vichnevetsky, R., "Treatment of Non-Linear Terms in Hyperbolic Equations," TR 70-23, Sept. 1970, Electronic Associates Inc., Princeton, N.J.

[26] Isaacson, E. and Keller, H. B., *Analysis of Numerical Methods,* Wiley, New York, 1966, pp. 58–61.

[27] Cohen, N. S., Derr, R. L., and Price, C. F., "Study of Ignition and Extinguishment in Multiple Stop-Restart Duty Cycles," *8th JANNAF Combustion Meeting,* Vol. II, CPIA Publication 220, Nov. 1971.